

SURFACE DEFORMATION MONITORING AND ANALYSIS IN XINJING MINING AREA BASED ON SBAS-INSAR TECHNOLOGY

FangZhou Fu

*College of Intelligent Mining Engineering, China University of Mining and Technology-Beijing, Beijing 100080, China.
Corresponding Email: 13007343782@163.com*

Abstract: Large-scale mining activities in mining areas can induce surface deformation phenomena, threatening the stability of peripheral production systems and residential environmental safety. Consequently, implementing high-precision surface deformation monitoring has become a critical component of mine safety assessment systems and ecological restoration projects. This study takes the Xinjing Mining Area in Alxa League, as a case study. Utilizing 20 scenes of Sentinel-1 ascending orbit images acquired from January 2022 to December 2023, this study applied the SBAS-InSAR technique for deformation monitoring and analysis. The results demonstrated complex deformation patterns in the Xinjing Mining Area during the study period, primarily characterized by subsidence. The deformation rate across the study area ranged from -125.8 mm/a to +36.3 mm/a, with cumulative deformation magnitudes ranging from -213.3 mm to +76.7 mm. The deformation process evolved through three distinct phases: an accelerated deformation phase, a moderate deformation phase, and a stabilization phase. This study provides essential data support and a scientific basis for preventing mining-induced subsidence caused by engineering activities in mining areas.

Keywords: SBAS-InSAR; Alxa open-pit coal mine; Surface deformation monitoring; Spatiotemporal evolution

1 INTRODUCTION

Mineral resource exploitation serves as the foundation supporting modern industrial development [1], yet the surface deformation it induces has become a global focus in mine environmental governance [2]. Processes such as open-pit excavation, underground goaf collapse, and groundwater level fluctuations can lead to surface deformation, ground fissure propagation, and even landslides, posing significant threats to mining safety and surrounding communities [3-4]. Although conventional monitoring techniques (e.g., GNSS and precise leveling) provide millimeter-level deformation accuracy [5-6], their low spatial density and high costs limit their applicability for large-scale dynamic monitoring in mining areas [7-8]. Consequently, high-resolution, wide-coverage remote sensing technologies for surface deformation monitoring hold urgent practical significance for mine hazard early warning and ecological restoration [9].

Interferometric Synthetic Aperture Radar (InSAR) technology, utilizing its all-weather and large-scale observational capabilities [10], has revolutionized deformation monitoring in mining areas. In recent years, time-series InSAR techniques such as SBAS-InSAR have significantly enhanced the accuracy and spatiotemporal continuity of deformation inversion by constructing optimized small-baseline interferometric networks. These advancements have demonstrate unique advantages in monitoring slow and nonlinear deformation [11-13]. Currently, this technology has been widely applied in multiple domains, including mine subsidence monitoring, surface settlement prediction, urban subsidence rate assessment, and spatiotemporal characteristic analysis of mining-induced deformation [14-15]. SBAS-InSAR, with its distinctive all-weather observation capability, continuous monitoring characteristics, and high spatial resolution and measurement precision, provides innovative technical solutions for unraveling the spatiotemporal evolution patterns of mining-induced subsidence [16].

A catastrophic collapse occurred at the Xinjing Coal Mine on February 22, 2023 [17], making time-series deformation monitoring of this mine critical for ensuring mining safety and public safety. While previous studies, notably by Ma et al. [18], have extensively documented the pre-slope-destabilization surface deformation patterns in the mining area, their conclusions remain constrained by the lack of systematic deployment of ground monitoring networks to validate deformation magnitudes, particularly in critical zones with high displacement gradients. Furthermore, existing literature predominantly focuses on pre-collapse deformation mechanisms, leaving the dynamic post-collapse evolution—such as stress redistribution and secondary instability risks—insufficiently resolved. To address these limitations, this study provides a comprehensive analysis of surface deformation spanning both pre- and post-avalanche phases. By integrating multi-temporal InSAR observations with post-event field validations, we systematically quantify the cascading impacts of slope failure on deformation regimes, thereby advancing a more holistic understanding of mining-induced geohazard progression. This study utilizes 20 Sentinel-1 ascending orbit images acquired from January 2022 to December 2023. Using SBAS-InSAR technology, we conducted deformation monitoring and analysis in the Xinjing Mining Area, thereby providing data support for preventing mining-induced subsidence caused by engineering activities.

2 STUDY AREA

The Xinjing open-pit coal mining area, a representative northern mining region, has faced escalating subsidence-related challenges, including recurrent landslides and agricultural land degradation, driven by decades of intensive extraction activities. The sparse vegetation coverage and geomorphological stability collectively ensure sufficient coherence for interferometric processing. Comprehensive mining records, hydrological datasets, and ground-based measurements are systematically archived, enabling robust cross-validation with InSAR-derived deformation results. This study's outcomes are expected to directly inform disaster prevention strategies and operational loss mitigation, thereby demonstrating dual significance in advancing subsidence mechanism research and promoting sustainable mining practices.

The Xinjing Coal Mine is located in the northwestern part of Alxa Left Banner, Alxa League, with geographical coordinates ranging from 105°30'E to 105°45'E and 39°10'N to 39°25'N, adjacent to the western foothills of the northern Helan Mountains. The mining area exhibits an irregular polygonal shape, extending approximately 7.2 km north-south and 4.5 km east-west, covering a total area of 32.4 km². It borders the Helan Mountain National Nature Reserve to the north and the Tengger Desert Marginal Ecological Restoration Project Area to the south, serving as a critical ecological node in the desert-oasis transition zone.

The mining area lies within the intermixing zone of Helan Mountain piedmont alluvial-proluvial fans and desert terrain, gently sloping from northwest to southeast with gradients of 2° – 5° and an average elevation of 1,328 meters. Surface coverage consists of Quaternary aeolian sand deposits (3 – 8 m thick), locally exposing Jurassic sandstone bedrock. The climate is characterized by a mid-temperate extreme arid continental regime, featuring an annual precipitation of 127 mm (primarily concentrated from July to September) and evaporation exceeding 2,800 mm. The mean annual temperature ranges between 8 – 10 °C, with summer extreme highs reaching 40 °C and winter lows dropping to -25 °C. The region experiences a mean annual wind speed of 4.2 m/s dominated by northwest winds, with an annual sandstorm frequency of 21 days.

Coal seams in the mining area demonstrate a distinct north-south strike orientation, with thickness gradually increasing from 20 meters in the north to 100 meters in the south, forming a stable coal distribution pattern as shown in the satellite image map (Figure 1). The coal-bearing strata belong to the Taiyuan Formation and Shanxi Formation, featuring average seam thicknesses of 8 – 15 meters, dip angles of 5° – 15°, and burial depths of 50 – 200 meters. The coal is primarily long-flame type with calorific values of 4,500 – 5,500 kcal/kg, medium ash content (18% – 25%), and medium sulfur content (1.2% – 1.8%), making it suitable for power generation and chemical industries.

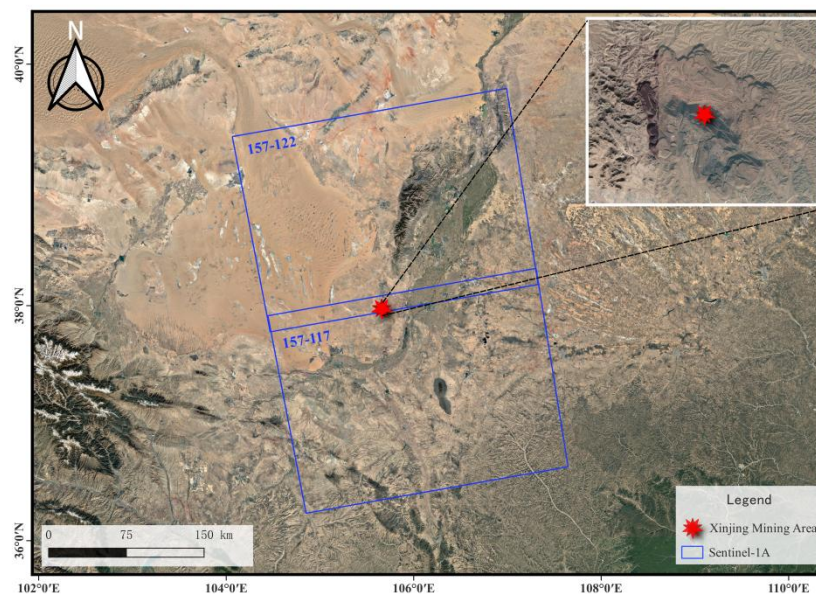


Figure 1 Overview Map of the Study Area

3 DATA AND METHODS

3.1 Data Source

To investigate surface deformation in the Xinjing Mining Area, this study employs radar satellite data for analysis. Sentinel-1A Synthetic Aperture Radar (SAR) data were acquired in Interferometric Wide (IW) swath mode with VV polarization, specifically utilizing Single Look Complex (SLC) products. A total of 20 Ascending orbit images spanning from January 7, 2022, to December 16, 2023, were selected for deformation analysis. Technical parameters of the Sentinel-1A imagery are detailed in Table 1. Additionally, the Shuttle Radar Topography Mission (SRTM) Digital Elevation Model (DEM) with 30 m spatial resolution was applied to compute topographic parameters, enabling precise geocoding and co-registration of SAR images.

Table 1 Parameters of SAR data

Data	Parameter	Description
Sentinel-1A	Time Span	2022/01/07~2023/12/16
	Data Volume	20
	Orbit Direction	Ascending
	Heading Angle	-13°11'
	Acquisition Mode	IW
	Polarization Mode	VV

3.2 SBAS-InSAR Methods

The SBAS-InSAR (Small Baseline Subset Interferometric Synthetic Aperture Radar) technique extract surface deformation information from multi-temporal SAR images by constructing a small-baseline interferometric network. This approach reduces decorrelation noise (e.g., coherence loss in vegetated areas) and improves data usability through the generation of phase interferograms. By selecting $N+1$ SAR scenes with uniform temporal spacing, M differential interferograms are generated based on predefined temporal and spatial baseline thresholds, where M satisfies the condition: $(N+1)/2 \leq M \leq N(N+1)/2$. The differential interferometric phase comprises contributions from deformation, residual topography, atmospheric delay, orbital errors, and noise, expressed mathematically as:

$$\Delta\varphi = \frac{4\pi}{\lambda} d(t) + \frac{4\pi B_{\perp}}{\lambda R \sin \theta} \Delta z + \varphi_{atm} + \varphi_{orb} + \varphi_{noise} \quad (1)$$

In the equation:

$\frac{4\pi}{\lambda} d(t)$ —Phase variation induced by surface deformation (target signal), where $d(t)$ represents the cumulative deformation displacement.

$\frac{4\pi B_{\perp}}{\lambda R \sin \theta} \Delta z$ —The phase residual induced by DEM elevation error Δz exhibits positive correlation with the vertical baseline B_{\perp} .

$\varphi_{atm}, \varphi_{orb}, \varphi_{noise}$ —Atmospheric delay phase (dominant error), orbital error phase, and noise-induced phase error.

The Sentinel-1 SAR datasets were processed using SBAS-InSAR techniques to derive millimeter-level accuracy time-series deformation fields and mean displacement velocity fields across the study area and its surroundings. Through these outputs, we analyzed the spatiotemporal evolution characteristics of surface deformation and revealed potential hazard development patterns. The technical workflow is illustrated in Figure 2.

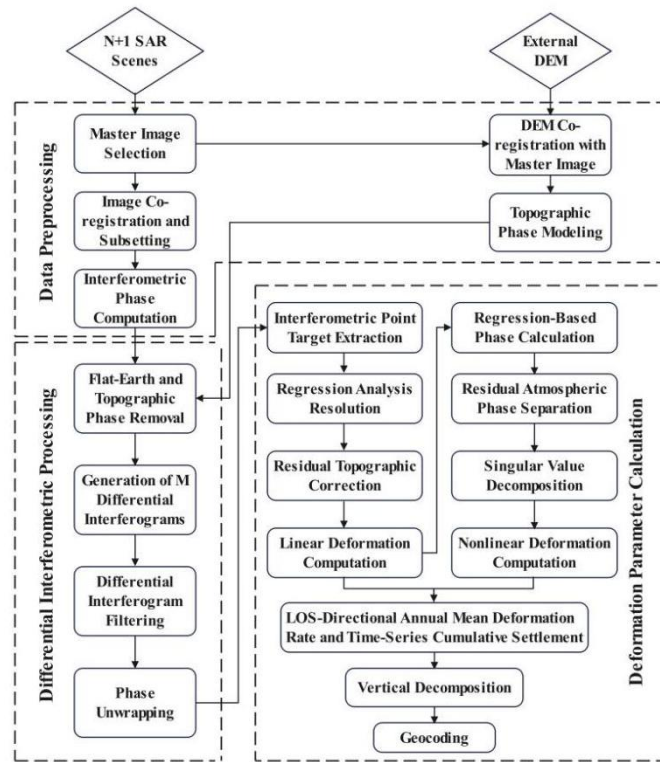


Figure 2 Technical Workflow Diagram

The key implementation steps are as follows:

(1) Master Image Selection:

A master image is selected from $N+1$ scenes by maximizing the overall coherence of all interferometric pairs. A multiplicative model evaluates four parameters: temporal baseline, spatial perpendicular baseline, Doppler centroid difference, and thermal noise. The image achieving maximum coherence is designated as the master to minimize co-registration errors and enhance alignment precision.

(2) Image Co-registration:

SAR slave images are co-registered to the master image to generate interferograms under spatiotemporal baseline constraints. To mitigate decorrelation caused by excessive baselines, a weighted least squares method with offset standard deviation weighting is implemented. Homologous points are identified via intensity cross-correlation or fringe sharpness algorithms, with weights assigned based on coherence values to solve offset polynomials. Precise orbit data and DEM-assisted range-Doppler modeling achieve sub-pixel alignment accuracy.

(3) Differential Interferogram Generation:

The flat-earth effect induces dense fringe patterns, complicating subsequent filtering and unwrapping. Prior to differential interferogram generation, SRTM-3 DEM data (30 m spatial resolution) is utilized to remove flat-earth and topographic phase contributions. Interferometric pairs are then selected based on temporal and spatial baselines, employing a multi-master image strategy to construct initial differential interferograms. Given the study area's complex geomorphology and significant topographic variations, high-quality interferograms are prioritized to mitigate residual topographic phase errors.

(4) Phase unwrapping:

The raw interferometric phase comprises not only surface deformation components but also residual orbital phases, topographic residuals, atmospheric delay phases, and noise. Due to the strong spatial randomness of topographic residuals and noise phases, direct unwrapping is infeasible. This study adopts a height-correction-based unwrapping approach. While height correction terms and noise phases exhibit spatial randomness, atmospheric delays and orbital residuals demonstrate spatial correlation. To address this, spatial-domain filtering is applied to estimate spatially correlated components, followed by adaptive filtering methods to remove these artifacts, yielding unwrapped interferograms. In areas with rapid land cover changes, significant topographic variations, or atmospheric coherence degradation, unwrapped interferograms still exhibit incomplete results in certain regions. Consequently, it is necessary to discard interferograms with poor unwrapping outcomes to ensure reliability in subsequent analyses.

(5) Deformation Estimation:

The unwrapped phase undergoes Singular Value Decomposition (SVD) to solve the least-squares problem for time-series deformation. Residual topographic phases and noise components (non-spatially correlated) are extracted by differencing the original unwrapped phases, enabling elevation correction and deformation sequence refinement. Deformation comprises linear and nonlinear components. Temporal filtering isolates time-correlated nonlinear deformation phases from uncorrelated atmospheric delays. The nonlinear deformation is then combined with spatially

filtered linear deformation to derive the final time-series deformation phase. The resulting line-of-sight (LOS) mean deformation rate and cumulative displacement time-series are vertically decomposed using the incidence angle. Subsequent geocoding transforms the results from SAR coordinates to the WGS84 geographic coordinate system, enabling spatial analysis of mining-induced subsidence patterns.

4 RESULTS ANALYSIS AND DISCUSSION

4.1 Surface Deformation Velocity in the Mining Area

By applying SBAS-InSAR techniques to 20 Sentinel-1A scenes acquired from January 7, 2022, to December 16, 2023, we generated the mean deformation rate map of the Xinjing Mining Area (Figure 3). In this map: Positive values (blue) denote ground movement toward the satellite, corresponding to uplift, while negative values (red) signify displacement away from the satellite, indicative of subsidence.

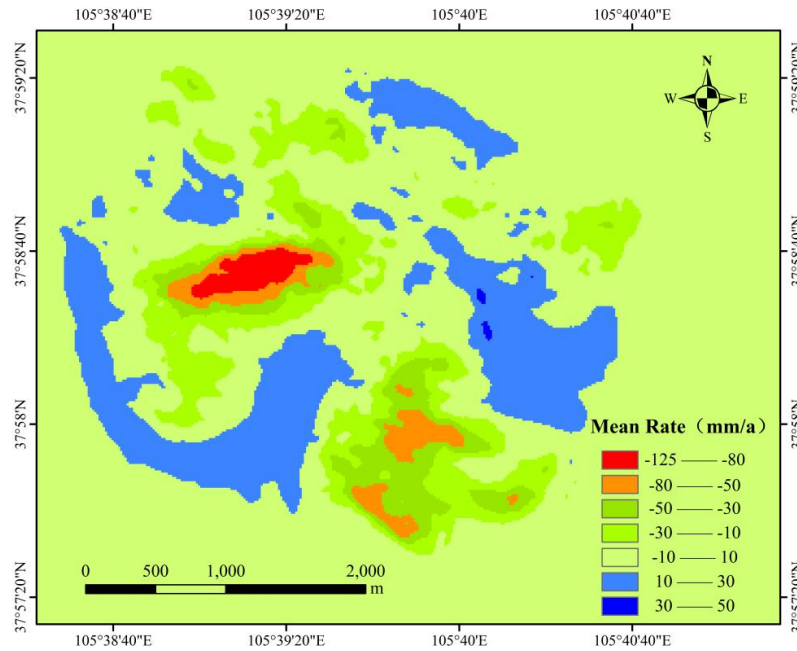


Figure 3 Mean Deformation Rate Map of the Xinjing Mining Area (2022 - 2023)

Figure 3 demonstrates pronounced surface deformation within the mining area, revealing distinct subsidence patterns across varying velocity ranges. Subsidence zones with rates of -125 to -80 mm/a cover 0.13 km² (4.9% of the total subsidence area), while those at -80 to -50 mm/a, -50 to -30 mm/a, and -30 to -10 mm/a occupy 0.28 km² (11.2%), 0.58 km² (23.3%), and 1.52 km² (60.6%), respectively. Notably, vertical uplift deformation (total area: 2.17 km²) is observed and preliminarily attributed to spoil material accumulation from open-pit mining operations.

4.2 Spatiotemporal Evolution of Surface Deformation in the Mining Area

To better investigate the spatiotemporal evolution characteristics of the mining area, this study obtained cumulative deformation displacements at different time intervals in the study area, as shown in Figure 4. The spatial evolution of deformation from 2022 to 2023 used January 7, 2022, as the reference baseline, with the surface deformation on that date set to 0 mm. Figure 5 demonstrates that from January to June 2022, the deformation distribution area in the study region significantly increased with accelerated deformation rates, resulting in cumulative displacements ranging from -142.0 mm to $+27.9$ mm. From July 2022 to March 2023, the deformation area continued to expand, though the rates slowed, with cumulative displacements reaching -213.1 mm to $+63.8$ mm. During the period from April to December 2023, the deformation process entered a relatively stable phase, with cumulative displacements showing only minor fluctuations between -213.3 mm and $+76.7$ mm. The spatiotemporal evolution reveals that the deformation extent expanded from 3.68 km² in June 2022 to 5.47 km² by November 2022, ultimately reaching 7.12 km² by December 2023. This evolutionary process clearly indicates that the surface deformation in the study area not only exhibits significant spatial expansion but also demonstrates continuous growth in cumulative displacement.

To further investigate deformation trends in the mining area, six representative feature points were selected in Figure 4, Record their deformation information in Table 2. And their cumulative deformation curves are plotted in Figure 5. Figure 5 reveals sustained growth trends in cumulative deformation across all monitoring points, with significant rate variations. Notably, point C2 exhibits the maximum cumulative deformation of -171.1 mm, while point C1 shows the minimum displacement at $+99.6$ mm.

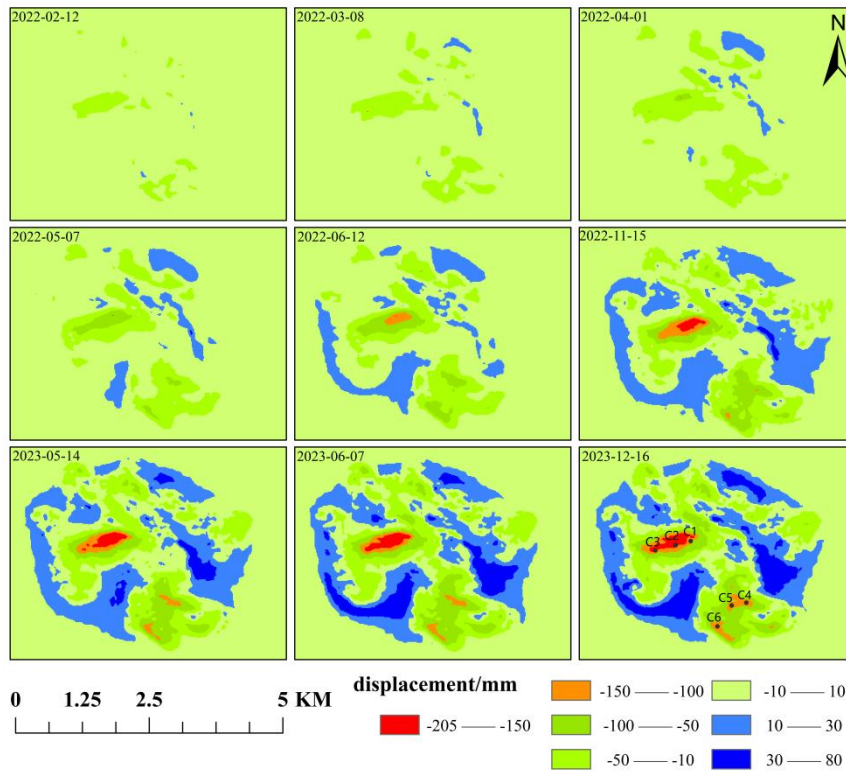


Figure 4 Spatiotemporal Deformation Evolution Map

Specifically, the temporal evolution characteristics of surface deformation at the six monitoring points can be broadly categorized into three distinct phases:

(1) Accelerated Deformation Phase: From January to June 2022, deformation rates at all six monitoring points increased substantially, with cumulative displacements growing progressively. During this period, point C2 exhibited the maximum deformation, reaching -99.5 mm by June 12, 2022, corresponding to an average deformation rate of -198.3 mm/a. In contrast, point C5 showed the minimum deformation, with a cumulative displacement of -44.3 mm and an average rate of -88.1 mm/a. The rapid deformation progression is directly attributable to high-intensity mining operations, which triggered abrupt stress redistribution in overburden strata.

(2) Moderate Deformation Phase: From July 2022 to March 2023, point C3 exhibited the maximum cumulative deformation of -66.8 mm with a mean deformation rate of -95.5 mm/a, while point C1 showed the minimum displacement (-27.5 mm, mean rate: -39.3 mm/a). Notably, a major landslide occurred on February 22, 2023, during the terminal phase of this period. Analysis of cumulative deformation curves reveals that the excessive deformation rates induced by sustained high-intensity stripping operations during Phase 1 directly triggered this disaster. Preceding the event, monitoring points C1, C2, and C3 exhibited daily subsidence rates exceeding 0.5 mm/day. Such rapid stripping rates promoted the formation of oversteepened slopes, with progressive stability degradation over time ultimately leading to slope failure.

(3) Stabilization Phase: From April to December 2023, deformation rates at all six monitoring points decelerated and gradually stabilized. During this period, only point C5 retained residual deformation of -37.6 mm, while displacements at other points remained within -20 mm. Notably, point C1 exhibited an anomalous reduction in cumulative deformation of 23.5 mm. These trends are closely linked to post-landslide mitigation measures, including production suspension, operational rectification, and slope reinforcement engineering. The stabilization demonstrates that anthropogenic interventions effectively suppressed further deformation progression.

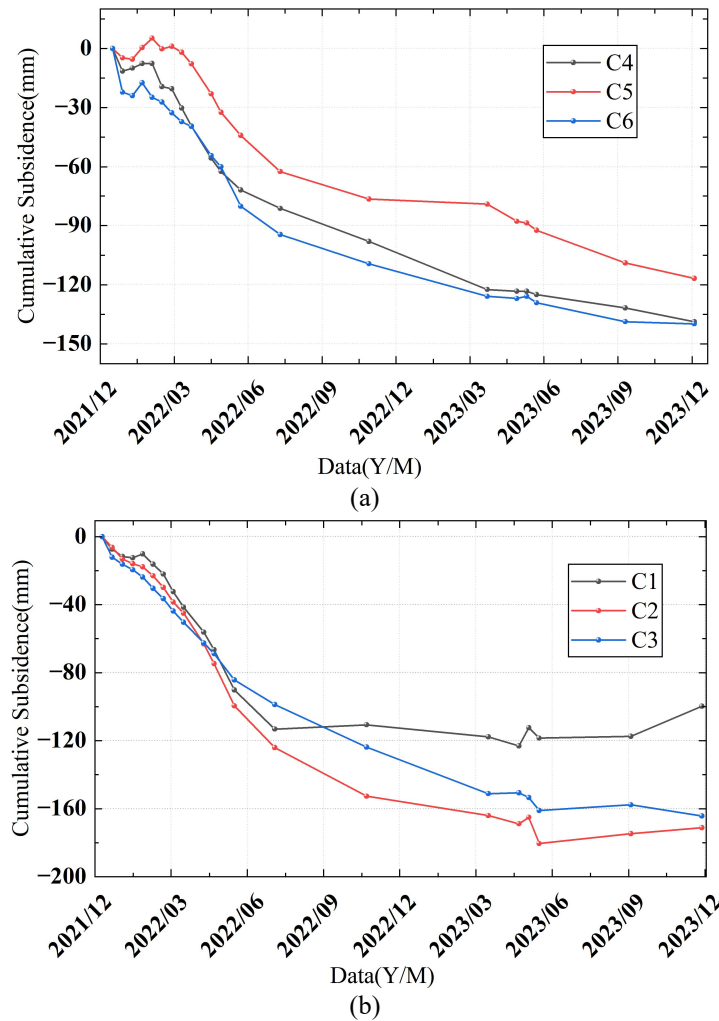


Figure 5 Cumulative Deformation Curve

Table 2 Deformation Information at Monitoring Points

Monitoring Points	Mean Deformation Rate (mm/a)	Cumulative Displacement (mm)	Maximum Displacement (mm)
C1	-51.9	-99.6	-123.1
C2	-89.3	-171.1	-180.4
C3	-85.7	-164.3	-165.8
C4	-72.3	-138.6	-138.6
C5	-60.8	-116.6	-116.6
C6	-72.9	-139.7	-140.1

5 CONCLUSIONS

This study employed time-series InSAR techniques to analyze 20 Sentinel-1 SAR images (2022-2023) covering the Xinjing Mining Area, deriving a mean deformation velocity field and revealing its spatiotemporal evolution patterns. The reliability of deformation monitoring results was cross-validated using optical remote sensing imagery. Key conclusions are as follows:

- (1) Areas with deformation rates of -10 to -30 mm/a account for 60.6% of the total subsidence zone, predominantly distributed along the periphery of the main deformation region. Rapid deformation zones (rates < -30 mm/a) cluster centrally, consistent with the "downward excavation and progressive convergence" mining pattern of open-pit operations, confirming data validity.
- (2) From January 2022 to December 2023, surface deformation in the Xinjing Mining Area progressed through three distinct phases: The first phase, spanning January to June 2022, was characterized by accelerated deformation, during which intense ground displacement occurred and the majority of cumulative subsidence in the mining area was generated. Subsequently, from July 2022 to March 2023, deformation entered a moderate phase marked by reduced rates of both subsidence velocity and cumulative displacement accumulation, significantly differing from the preceding period. The final stabilization phase, lasting from April to December 2023, exhibited minimal deformation magnitudes, including localized uplift anomalies in cumulative displacement. These stabilization trends are attributed to the successful implementation of post-landslide mitigation measures, including operational suspension and slope

reinforcement engineering, which effectively suppressed further deformation progression.

(3) InSAR technology effectively monitors mining-induced surface deformation, providing critical data support for hazard prevention and serving as a vital bridge between geohazard mechanism research and engineering practices. Its application significantly enhances mine safety management and disaster mitigation capabilities.

COMPETING INTERESTS

The authors have no relevant financial or non-financial interests to disclose.

REFERENCES

- [1] T Muhammad, G Ni, Z Chen, et al. Addressing resource curse: How mineral resources influence industrial structure dynamics of the BRI 57 oil-exporting countries. *Resources Policy*, 2024, 99: 105420.
- [2] Z Luo, L Zhou, J Qin, et al. Assessing surface deformation in the Chengdu Plain: A comprehensive time-series InSAR study of urban development and natural environmental factors. *Advances in Space Research*, 2024, 73(3): 1780–1798.
- [3] J Geng, X Zhang, J Lin, et al. 3S technology and its application in the assessment and monitoring of mining geological disasters. *Digital Technology and Application*, 2013, (04): 93–95.
- [4] H Kawabata, S Yoshioka. Spatiotemporal changes in the strain field in the Niigata-Kobe Tectonic Zone: long-term analysis using GNSS time series data. *Progress in Earth and Planetary Science*, 2025, 12(1): 22–22.
- [5] M D Lucio, C Riccardo, C Valentina, et al. Integrated approaches for field mapping by traditional investigation and satellite PSInSAR data: Results from the Montemartano Landslide (Central Italy). *Remote Sensing*, 2023, 15(5): 1221–1221.
- [6] K Zhang, Q Li, H Dai, et al. Research on the integrated monitoring technology of “air and sky” for surface movement in mining area. *Coal Science and Technology*, 2020, 48(02): 207–213.
- [7] J Huang, B Wang, X Cai, et al. Coastal reclamation embankment deformation: Dynamic monitoring and future trend prediction using multi-temporal InSAR technology in Funing Bay, China. *Remote Sensing*, 2024, 16(22): 4320–4320.
- [8] D Zhou, X Zuo. Surface deformation monitoring and prediction in mining area based on SBAS-InSAR and PSO-BP neural network algorithm. *Journal of Yunnan University (Natural Science Edition)*, 2021, 43(05): 895–905.
- [9] E Bayramov, N Sydyk, S Nurakynov, et al. Quantitative assessment of urban surface deformation risks from tectonic and seismic activities using multitemporal microwave satellite remote sensing: A case study of Almaty city and its surroundings in Kazakhstan. *Frontiers in Built Environment*, 2024, 10: 1502403.
- [10] Q Fan, C Tang, Y Chen, et al. Application of GPS and InSAR technology in landslide monitoring. *Surveying and Mapping Science*, 2006(05): 60–62+5.
- [11] K E, A N, F H, et al. Monitoring of land surface displacement based on SBAS-InSAR time-series and GIS techniques: A case study over the Shiraz metropolis, Iran. *ISPRS Annals of the Photogrammetry, Remote Sensing and Spatial Information Sciences*, 2023, X-4/W1: 371–378.
- [12] R Wang, S Xiong, H Nie, et al. Research on remote sensing geological survey technology and application. *Journal of Geology*, 2011, 85(11): 1699–1743.
- [13] M Manunta, D C Luca, I Zinno, et al. The Parallel SBAS approach for Sentinel-1 interferometric wide swath deformation time-series generation. Algorithm description and products quality assessment. *IEEE Transactions on Geoscience and Remote Sensing*, 2019, 57(9): 6259–6281.
- [14] H Yin, J Zhu, C Li, et al. Research on deformation monitoring of mining area based on SBAS. *Journal of Surveying and Mapping*, 2011, 40(01): 52–58.
- [15] Q Yang, P Xu, C Cao, et al. Research on land subsidence prediction in mining areas based on SBAS-InSAR and multi-model comparison. *Journal of Research in Science and Engineering*, 2024, 6(12): 63–71.
- [16] A Mugabushaka, Z Li, X Zhang, et al. Mapping surface deformation in Rwanda and neighboring areas using SBAS-InSAR. *Remote Sensing*, 2024, 16(23): 4456–4456.
- [17] W Shen. Mindful of people's well-being, dedication to escort a better life. *China Mining News*, 2024(001).
- [18] F Ma, R Li, X Liu, et al. Surface settlement monitoring of Xinjing coal mine based on time series InSAR technology. *Journal of Shanxi Datong University (Natural Science Edition)*, 2023, 39(04): 123–127.